J. Fluid Mech. (2024), *vol*. 987, A11, doi:10.1017/jfm.2024.332

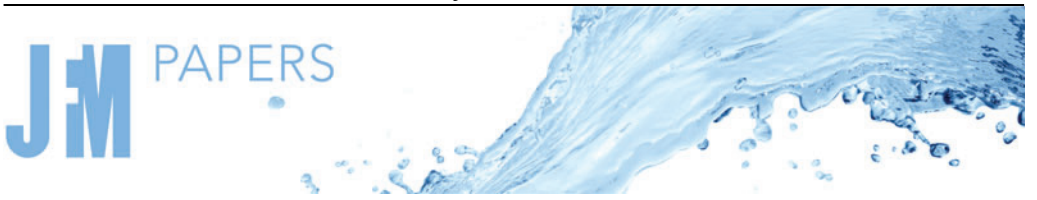

Starting vortices generated by an arbitrary solid body with any number of edges

Edward M. Hinton[1], **A. Leonard**[2], **D.I. Pullin**[2] **and John E. Sader**[2,3],†

[1]School of Mathematics and Statistics, The University of Melbourne, Victoria 3010, Australia

[2]Graduate Aerospace Laboratories, California Institute of Technology, Pasadena, CA 91125, USA

[3]Department of Applied Physics, California Institute of Technology, Pasadena, CA 91125, USA

(Received 3 September 2023; revised 27 March 2024; accepted 30 March 2024)

The starting vortex generated at the trailing edge of a flat plate, that is impulsively translated at fixed angle of attack, is a widely studied canonical problem. Recent work that examined the effect of plate rotation on this starting vortex found that two new and distinct vortex sheet types can arise. We generalise this work to study the starting vortex generated at any sharp and straight edge of an arbitrary body under a general time-dependent two-dimensional motion. The dimensionless velocity field of the attached flow near any sharp edge is assumed to take the form, $\hat{z}^{-1/2}f(T) + g(T) + o(1)$, where $\hat{z}$ is the dimensionless position referenced to the edge, $f(T)$ and $g(T)$ are functions of dimensionless time, T, associated with the local flow perpendicular and parallel to the edge, respectively. This enables starting vortices to be generally calculated and their types related by simply inspecting the forms of $f(T)$ and $g(T)$. We elucidate the physics underlying all three vortex types and show that these vortices are generated by pure translation of the sharp edge. Several case studies are explored, including the leading/trailing edge vortices of a flat plate which can simultaneously be of different type (relevant to low-speed aircraft), the vortex formed by translation of a semi-infinite flat plate and the trailing-edge vortex of Joukowski aerofoils. With the ability to calculate the vortices at all edges, the theory is used to develop a general formula for the lift force of a flat plate which can find application in practice.

Key words: vortex dynamics, vortex shedding

1. Introduction

The sudden (or start up) motion of a solid body immersed in a viscous fluid can generate vortices that are convected away from the body as the flow evolves. This vortex generation often provides a dominant contribution to the lift experienced by the body and, hence, its

† Email address for correspondence: jsader@caltech.edu

characterisation is essential in practice. The physical processes underlying this generation have been the subject of intensive research over the past century due to their importance in aerodynamics (Prandtl 1921; Graham 1983; Pullin & Wang 2004; Jones & Babinsky 2010). The form of the starting vortex and its sensitivity to its surrounding (irrotational) flow field are also used in nature, e.g. to optimise locomotion of insects or for the propulsion of blood within the heart (Gharib, Rambod & Shariff 1998). More fundamentally, the unsteady dynamics of the starting vortex is a canonical problem of longstanding importance in fluid dynamics.

Theoretical calculation of the starting vortex has traditionally centred on the property that, at early times, it remains close to the solid body. For generation at a sharp edge of the body, where an inviscid formulation allows for the Kutta condition (Crighton 1985) to be imposed, the vortex dynamics are independent of the body's length scale. This has motivated self-similar solutions that have been widely reported in the literature (Prandtl 1921; Kaden 1931; Alexander 1971; Pullin 1978). These calculations have generally focused on (i) vortex sheet formulations, in which the fluid velocity is discontinuous across the sheet, and (ii) point vortex approaches that localise the generated vorticity at singular points in space (Cortelezzi & Leonard 1993; Krasny & Nitsche 2002; Jones 2003; Tchieu & Leonard 2011). The former approach is more readily compared with experiment where it is assumed to be an infinite Reynolds number approximation. Importantly, the starting vortex may exhibit a Kelvin–Helmholtz-like instability that breaks the self-similarity implicit in these vortex sheet formulations (Moore 1975; Krasny & Nitsche 2002; Luchini & Tognaccini 2002).

Extensive numerical investigations of the starting vortex generated at a sharp edge, that also invoke an inviscid formulation, have been reported. These include finite-difference algorithms (Xu & Nitsche 2015), boundary integral methods (Jones 2003) and particle-based methods (Eldredge 2007). All these studies recover the self-similar behaviour reported above at small time, along with its breakdown at longer times. Experiments have shown that the inviscid self-similar theory at small time provides a robust representation of vortex formation in a real viscous fluid, even at moderate Reynolds numbers (Pullin & Perry 1980).

The ability to compute the starting vortex provides access to the calculation of the (vortex-induced) lift experienced by the solid body at small time, i.e. just after start up. For example, Pullin & Wang (2004) showed that the leading-order contribution to this force, in the particular case of pure translation of a flat plate at small angle of attack, can be computed from the similarity solution for the trailing-edge vortex alone. This was compared to the classical solution of Wagner (1925), where agreement was observed. At larger angles of attack, the leading-edge vortex on the plate can enhance lift and this has also been quantified experimentally (Pitt Ford & Babinsky 2013).

Pullin & Sader (2021), henceforth denoted PS21, formulated a class of similarity solutions for the starting vortex at the trailing edge of a flat plate that simultaneously translates and rotates. The plate's translational and rotational velocities were specified by separate power laws of time. This produced a governing system for the vortex sheet in the vicinity of the trailing edge of the plate, in terms of the similarity variables, that accounted for the attached flow and vortex-image self-induction. For zero initial angle of attack, they identified three distinct vortex types: (i) type I is the vortex sheet reported by Pullin (1978), which is dominated by plate rotation with a Kaden spiral at its centre (Kaden 1931); (ii) type II is a flat vortex sheet (without roll up), that is parallel to and rotates with the plate, which is driven by convection parallel to the edge; and (iii) type III combines these effects and arises when the physical ingredients that dominate each of the first two

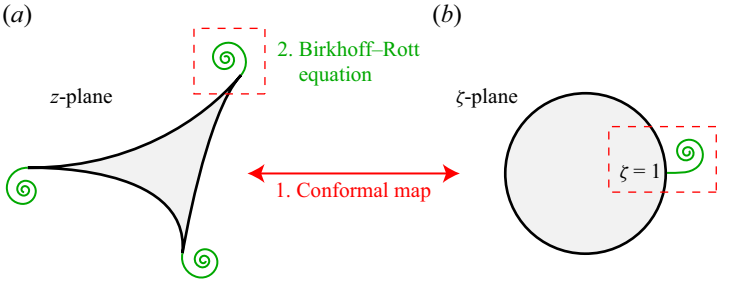

Figure 1. Schematic showing an (arbitrary) solid body in the physical z-plane (a), and the vortices formed at its sharp and straight edges. The exterior of the arbitrary body (white region) is conformally mapped onto the exterior of a circle in the ζ-plane (b); the edge under consideration in the z-plane is mapped onto $\zeta = 1$ (dashed red boxes). This mapping enables calculation of the attached exterior flow generated by the solid body and the self-induced velocity of the vortex sheet. The image vortex sheet inside the body in the z- and ζ-planes, required to satisfy the no-penetration condition, is not shown.

types are in balance. Strikingly, only type-III vortices depend on the relative magnitude of plate translation-to-rotation velocities, with their form generally morphing from type-I like to type-II like as the translational velocity of the plate increases. Type-II and type-III vortex sheets are new to the literature and their existence in a real viscous flow are yet to be confirmed; this is the subject of a separate study (Sader *et al.* 2024).

The aim of the present study is to calculate the starting vortex generated at the sharp and straight edge, i.e. one in which the surfaces immediately adjacent to the edge are parallel, of a general body undergoing a general start-up motion; see figure 1. The universal dynamics of the starting vortex are formulated, which depend solely upon two (arbitrary) functions of time in the velocity field for the local attached flow, i.e. in the vicinity of the edge. The primary assumptions are that the flow is inviscid and that time is small so that the vortex remains close to the edge. Under these assumptions, the vortex dynamics depend only on the local attached flow. That is, there is no need to solve the Birkhoff–Rott equation to identify the vortex type that will be generated. The three vortex types of PS21 are shown to occur generally for a wide range of bodies and flows. This, in turn, provides new physical insights into the vortex dynamics. In so doing, the present study reports a unification of, and describes the relationship between, the dynamics of starting vortices generated by different geometries (e.g. Pullin 1978; Cortelezzi & Leonard 1993; Pullin & Sader 2021). Comparison of the present inviscid theory with direct numerical simulations of the Navier–Stokes equations at high Reynolds numbers is reported in Sader *et al.* (2024).

The study is organised as follows. In § 2, the general form of the velocity field for the attached flow local to a sharp and straight edge is reported. The two leading-order terms with respect to distance from the edge are retained and denoted $f(T)$ and $g(T)$, where T is the dimensionless convective time (defined in the following). We show that, under a general power law in time motion, the self-similar dynamics of the starting vortex are governed solely by the time dependencies of $f(T)$ and $g(T)$, falling into one of the three vortex types reported by PS21. We show that the vortex type is determined by the competition between the two functions, $f(T)$ and $g(T)$, which are associated with the local flow perpendicular and parallel to the edge, respectively. Several case studies are examined in § 3, elucidating the dominant flow physics and demonstrating the broad applicability of the formulation. This includes calculation of the leading-edge vortex of a flat plate, i.e. all vortices of a flat plate are derived, and vortices generated at the trailing edge of Joukowski aerofoils. The dynamics of these different case studies are also related to each other

through the general expansion of the attached flow in terms of $f(T)$ and $g(T)$. This provides insight into the underlying fluid physics that leads to the generation of type-I, type-II and type-III vortices. We show that different vortex types can exist at the leading and trailing edges of a flat plate, under special yet practically relevant circumstances. This is relevant to model aeroplanes and other low-speed aircraft, such as micro air vehicles (MAVs) and unmanned air vehicles (UAVs), as we discuss. We also determine the minimal velocity components of a moving flat plate that give rise to the three vortex types. Calculation of both the leading- and trailing-edge vortices of a flat plate enables determination of the lift force, which is reported in § 4. Concluding remarks are made in § 5 with derivation details relegated to Appendix A.

2. General theory for any straight edge of a solid body

We consider a rigid solid body of arbitrary shape that is immersed in an unbounded inviscid fluid. The body has a finite number of sharp edges, each with an exterior angle of π, i.e. the two surfaces of the body immediately adjacent to each edge are straight and parallel. The aim is to calculate the starting vortex generated at each sharp and straight edge, which is performed independently of all other edges. This approach is rigorous in the small-time limit (Pullin 1978).

2.1. *Attached flow around a rigid solid body*

The complex (dimensional) z-plane, $z = x + \mathrm{i}y$, where i is the imaginary unit, is fixed to the moving frame of the rigid solid body; see figure 1. The origin of this (x, y) frame is centred at the edge whose starting vortex is to be calculated with its x-axis parallel to, and directed away from, the solid body surfaces immediately adjacent to this edge. This local Cartesian frame is oriented to form a three-dimensional right-handed coordinate system, whose third (unnamed) basis vector is orthogonal to the z-plane and points in the same direction at each edge, e.g. out of the page in figure 1. The exterior of the rigid solid body (white region in figure 1) in the z-plane is conformally mapped onto the exterior of a circle which occupies the (dimensionless) ζ-plane (right-hand diagram in figure 1) with its origin at the centre of the circle. The edge under consideration at $z = 0$ is mapped onto $\zeta = 1$. The z-frame is non-dimensionalised,

$$z = \mathcal{L}\hat{z}, \tag{2.1}$$

where $\mathcal{L}$ is the characteristic length scale of the flow field, i.e. the size of the solid body, and $\hat{z}$ is dimensionless. Close to this edge, i.e. $|\hat{z}| \ll 1$, the conformal mapping takes the form

$$\zeta = 1 + c_{1/2}\hat{z}^{1/2} + c_1\hat{z} + o\big(|\hat{z}|\big), \tag{2.2}$$

where the $c_{1/2}$ and c_1 are non-zero constants that depend on the body's geometry only. The constant $c_{1/2}$ is real by construction of the conformal map. The dimensionless velocity potential for the flow generated by the body motion, termed the 'attached flow', can be expressed in its Laurent series:

$$W_a(\zeta, T) = \sum_{n=-\infty}^{\infty} a_n(T)\zeta^n, \tag{2.3}$$

where $T = t/\mathcal{T}$ is dimensionless time and $\mathcal{T}$ is the (convective) timescale for the flow, e.g. the size of the solid body divided by the velocity scale for its motion, and the functions of time, $a_n(T)$, are specified by the particular solid body and its motion.

Substituting (2.2) into (2.3), and expanding for small $\hat{z}$, yields

$$W_a(\hat{z}, T) = 2\hat{z}^{1/2} f(T) + \hat{z} g(T) + \text{higher order}, \tag{2.4}$$

giving the velocity field local to the edge under consideration,

$$u_a - \mathrm{i} v_a \equiv \frac{\partial W_a}{\partial \hat{z}} = \hat{z}^{-1/2} f(T) + g(T) + \text{higher order}, \tag{2.5}$$

where u_a and v_a are the corresponding velocity components in the x- and y-directions, respectively, $f(T)$ and $g(T)$ are functions of time specified by motion of the body (which absorb the coefficients and time-dependent functions in (2.2) and (2.3)), and we have omitted terms in (2.4) that do not depend on $\hat{z}$ because they do not contribute to the velocity field. The form of the attached flow in (2.5) is assumed henceforth, with $f(T)$ and $g(T)$ being the quantities of primary interest in the developed theory. The function, $f(T)$, is associated with the local flow perpendicular to the straight edge, whereas $g(T)$ is parallel to the edge.

As we show in § 3, the two leading-order terms in (2.5) are as specified for several cases of practical interest. Moreover, we are unable to identify an attached flow around a physically realisable solid body of finite extent, whose local flow at one of its edges exhibits higher-order terms in (2.5) that are important. A flow in which the higher-order terms in (2.5) play a dominant role, if it were to exist in reality, may result in vortex dynamics that are not described by the present theory.

2.2. *Birkhoff–Rott equation for evolution of a vortex sheet*

The vortex sheet generated by (2.5) in the z-plane is parameterised by

$$\hat{z} = \hat{z}_v(\Gamma, T), \tag{2.6}$$

where the Lagrangian variable, Γ, is a dimensionless circulation (scaled by $\mathcal{L}^2/\mathcal{T}$) that gives the total amount of circulation between a point on the vortex sheet and its free end, and the subscript, v, refers to the vortex sheet.

The vortex sheet obeys the Birkhoff–Rott evolution equation (Rott 1956; Birkhoff 1962; Saffman 1995),

$$\left(\frac{\partial \bar{\hat{z}}_v}{\partial T}\right)_{\Gamma} = u_a - \mathrm{i} v_a + u_v - \mathrm{i} v_v, \tag{2.7}$$

where the overbar indicates the complex conjugate, and $u_v - \mathrm{i} v_v$ is the dimensionless velocity field induced by the sheet's interaction with the solid body. This self-induced velocity field guarantees zero total circulation via Kelvin's circulation theorem, and is given by (Milne-Thomson 1996)

$$u_v - \mathrm{i} v_v = -\left(\frac{\partial \zeta}{\partial \hat{z}}\right)_{\hat{z}_v} \frac{1}{2\pi \mathrm{i}} \fint_{\Gamma_0(T)}^{0} \left(\frac{1}{\zeta_v - \zeta_v'} - \frac{1}{\zeta_v - \dfrac{1}{\bar{\zeta}'_v}} \right) \mathrm{d}\Gamma', \tag{2.8}$$

where the integral denotes the Cauchy principal value, $\zeta_v \equiv \zeta(z_v(\Gamma, T))$, $\zeta_v' \equiv \zeta(z_v(\Gamma', T))$, and $\Gamma_0(T)$ is the total circulation shed at time, T.

From (2.2) and (2.5), it follows that the evolution equation for the vortex sheet is

$$\left(\frac{\partial\bar{\hat{z}}_v}{\partial T}\right)_{\Gamma} = \hat{z}_v^{-1/2} f(T) + g(T) - \frac{1}{4\pi \mathrm{i}}\hat{z}_v^{-1/2}\int_{\Gamma_0(T)}^{0}\left(\frac{1}{\hat{z}_v^{1/2} - \hat{z}_v'^{1/2}} - \frac{1}{\hat{z}_v^{1/2} + \bar{\hat{z}}_v'^{1/2}}\right)\mathrm{d}\Gamma', \tag{2.9}$$

where the dash indicates dependence on Γ' (as in (2.8)), and we have not included the $O(1)$ contributions from the integral in (2.8) because they are always subdominant in the vortex dynamics (as in PS21). The Kutta condition is used to regularise the solution by removing the (unphysical) velocity singularity at the sharp edge, $\hat{z}_v = 0$ (Crighton 1985). This captures the behaviour of a (real) viscous fluid, where viscous diffusion guarantees that the velocity field is always finite. That is, the Kutta condition requires the term of $O(\hat{z}_v^{-1/2})$ in (2.9) to vanish at the edge, i.e. as $\hat{z}_v \to 0^+$, which gives the auxiliary condition,

$$f(T) + \frac{1}{4\pi \mathrm{i}}\int_{\Gamma_0(T)}^{0}\left(\frac{1}{\hat{z}_v'^{1/2}} + \frac{1}{\bar{\hat{z}}_v'^{1/2}}\right)\mathrm{d}\Gamma' = 0. \tag{2.10}$$

2.3. *Self-similar evolution of the vortex sheet generated at an edge*

We calculate the evolution of the vortex sheet generated at each edge of the body, immediately following start up, i.e. $T \ll 1$. Motion of the solid body is assumed to obey a power-law dependence on time. It then follows that

$$f(T) = \mathrm{i} f_0 T^k + o\left(T^k\right), \quad g(T) = g_0 T^l + o\left(T^l\right), \tag{2.11a,b}$$

where the power laws, $k, l \geqslant 0$, are related to the power laws of the body motion, and f_0 and g_0 are nonzero (complex) constants. The imaginary unit has been added to the first equation for notational convenience; see below.

The attached flow in (2.5) is devoid of any geometric length scale, enabling the generation of a vortex sheet of similarity form (Pullin 1978),

$$\hat{z}_v = T^q Z(\lambda), \quad \lambda = 1 - \frac{\Gamma}{\mathcal{J}T^s}, \tag{2.12a,b}$$

where the real-valued non-negative power laws, q and s, are to be determined, and $\mathcal{J}$ is a shed circulation constant defined by

$$\Gamma_0(T) = \mathcal{J}T^s. \tag{2.13}$$

Equations (2.11a,b) and (2.13) give $0 \leqslant \lambda \leqslant 1$, with $\lambda = 0$ and 1 coinciding with the sharp edge of the solid body and the vortex sheet's free end, respectively, i.e.

$$Z(0) = 0. \tag{2.14}$$

The Kutta condition in (2.10) becomes

$$f_0 T^k + \frac{\mathcal{J}}{4\pi}T^{s-q/2}\int_0^1\left(\frac{1}{Z'^{1/2}} + \frac{1}{\bar{Z}'^{1/2}}\right)\mathrm{d}\lambda' = 0, \tag{2.15}$$

and it follows that f_0 must be real valued. Equation (2.15) furnishes the following relation between the exponents,

$$s - \frac{q}{2} = k, \tag{2.16}$$

and simplifies to give

$$f_0 + \frac{\mathcal{J}}{4\pi}\int_0^1 \left(\frac{1}{Z'^{1/2}} + \frac{1}{\bar{Z}'^{1/2}}\right) \mathrm{d}\lambda' = 0. \tag{2.17}$$

This allows the governing equation in (2.9) to be recast as

$$T^{q-1}\left(q\bar{Z} + s(1-\lambda)\frac{\mathrm{d}\bar{Z}}{\mathrm{d}\lambda}\right) = \mathrm{i}\, Z^{-1/2} T^{s-q} f_0\,(1 + M(Z)) + g_0 T^l, \tag{2.18}$$

where

$$M(Z) \equiv \frac{\displaystyle\int_0^1 \left(\frac{1}{Z^{1/2} - Z'^{1/2}} - \frac{1}{Z^{1/2} + \bar{Z}'^{1/2}}\right) \mathrm{d}\lambda'}{\displaystyle\int_0^1 \left(\frac{1}{Z'^{1/2}} + \frac{1}{\bar{Z}'^{1/2}}\right) \mathrm{d}\lambda'}. \tag{2.19}$$

Equation (2.18) governs the entire dynamics of the vortex sheet generated at the edge.

The form of (2.18) shows that these dynamics are controlled by the relative strength of the two terms on its right-hand side, i.e. the power laws in time, $s - q$ and l. This establishes the existence of three possible vortex types, which we explore in the next section. The analysis generalises the recent work of PS21, who studied the trailing-edge vortex generated by a flat plate undergoing translation and rotation, to an arbitrary body with any number of edges that is executing arbitrary power-law-in-time motion.

2.4. *Three possible vortex sheet types*

The first term on the right-hand side of (2.18) arises from self-induction of the vortex sheet accounting for the presence of the solid body, the Kutta condition and flow perpendicular to the edge. In contrast, the second term is due to pure translation of the attached flow parallel to the straight edge, cf. (2.5), (2.11*a*,*b*) and (2.18). This gives rise to three separate vortex sheet types, depending on whether these terms balance or individually dominate the right-hand side of (2.18).

2.4.1. *Type-I vortex sheet*

Consider when the first term on the right-hand side of (2.18) dominates the second term, i.e.

$$l > s - q. \tag{2.20}$$

Balancing the left-hand side of (2.18) with its right-hand side, and using (2.16), produces

$$s = \frac{4k+1}{3}, \quad q = \frac{2k+2}{3}. \tag{2.21a,b}$$

Equation (2.20) then gives the corresponding condition on the power laws for the attached flow,

$$l > \frac{2k-1}{3}, \tag{2.22}$$

with the governing equation (2.18) becoming

$$\frac{2k+2}{3}\bar{Z} + \frac{4k+1}{3}(1-\lambda)\frac{\mathrm{d}\bar{Z}}{\mathrm{d}\lambda} = \mathrm{i}\, Z^{-1/2} f_0\,(1 + M(Z))\,, \tag{2.23}$$

which is to be solved subject to its initial condition (2.14); this can be performed numerically, as per PS21.

The dimensionless velocity jump across the vortex sheet, at any spatial position parameterised by λ, is

$$\gamma = \left|\frac{\mathrm{d}\Gamma}{\mathrm{d}\lambda}\right| \Big/ \left|\frac{\mathrm{d}\hat{z}_v}{\mathrm{d}\lambda}\right| = \mathcal{J}T^{(2k-1)/3}\left|\frac{\mathrm{d}Z}{\mathrm{d}\lambda}\right|^{-1}, \tag{2.24}$$

which is singular as $T \to 0$, for $0 \leqslant k < 1/2$, i.e. the velocity jump decays as time evolves. This is in contrast to $k > 1/2$ where the velocity jump is zero initially and grows monotonically, or it is independent of time and finite for $k = 1/2$. Note that $k = 0$ corresponds to an impulsive start-up flow, with increasing values of k providing a more gradual acceleration at early times. Physically, $0 \leqslant k < 1/2$ produces a strong concentration of vorticity at the plate edge which may be expected for an impulsive (or near impulsive) start-up flow. The situation resolves for $k \geqslant 1/2$.

2.4.2. *Type-II vortex sheet*

Next, we consider the complementary case where the second term dominates the first in the right-hand side of (2.18), i.e.

$$l < \frac{2k-1}{3}. \tag{2.25}$$

Balancing the left- and right-hand sides of (2.18), and using (2.16), then gives

$$s = k + \frac{l+1}{2}, \quad q = 1 + l. \tag{2.26a,b}$$

The canonical function, $f(T)$, in (2.5) for the attached velocity field is subdominant in this regime, and so the condition of no-penetration on the plate becomes

$$\mathrm{Im}\,\{g(T)\} = 0, \tag{2.27}$$

where Im denotes the imaginary component, i.e. g_0 in (2.11*a*,*b*) is real valued.

The governing equation for Z becomes

$$(1+l)\bar{Z} + \left(k + \frac{l+1}{2}\right)(1-\lambda)\frac{\mathrm{d}\bar{Z}}{\mathrm{d}\lambda} = g_0. \tag{2.28}$$

The corresponding initial condition for Z, and the Kutta condition, remain unchanged from (2.14) and (2.17), respectively.

This has exact analytical solution (cf. PS21),

$$Z = \frac{g_0}{1+l}\left(1 - (1-\lambda)^B\right), \tag{2.29}$$

where

$$B = \frac{2(1+l)}{1+l+2k} < 1, \tag{2.30}$$

Importantly, this type-II vortex sheet, which is a straight line geometrically, cannot be coincident with the solid edge under consideration. This condition imposes the constraint, $g_0 > 0$, which is illustrated in § 3.

The Kutta condition (2.17) gives

$$\mathcal{J} = -2f_0 g_0^{1/2} \sqrt{\frac{\pi}{1+l}} \frac{\Gamma_c\left(1+\dfrac{k}{1+l}\right)}{\Gamma_c\left(\dfrac{3}{2}+\dfrac{k}{1+l}\right)}, \tag{2.31}$$

where $\Gamma_c(\cdot)$ is the gamma function (not circulation).

The corresponding velocity jump across the vortex sheet is

$$\gamma = T^{k-(1+l)/2} \frac{\mathcal{J}}{g_0} \left(k+\frac{1+l}{2}\right) (1-\lambda)^{1-B}, \tag{2.32}$$

which can be expressed in terms of the spatial X-coordinate, where $Z = X + \mathrm{i}Y$, using (2.11*a*,*b*), to give

$$\gamma = T^{k-(1+l)/2} \frac{\mathcal{J}}{g_0} \left(k+\frac{1+l}{2}\right) \left(1-\frac{1+l}{g_0}X\right)^{(1-B)/B}. \tag{2.33}$$

2.4.3. *Type-III vortex sheet*

The final vortex type occurs when all terms on the right-hand side of (2.18) balance, i.e.

$$l = \frac{2k-1}{3}, \tag{2.34}$$

for which the governing equation (2.18) becomes

$$\frac{2k+2}{3}\bar{Z} + \frac{4k+1}{3}(1-\lambda)\frac{\mathrm{d}\bar{Z}}{\mathrm{d}\lambda} = \mathrm{i}\, Z^{-1/2} f_0 \left(1+M(Z)\right) + g_0, \tag{2.35}$$

whose form of solution now depends qualitatively on f_0 and g_0; this property is absent from type-I and type-II vortex sheets. Type-III vortices resemble type-I or type-II vortices in the cases that $f_0 \gg g_0$ or $g_0 \gg f_0$, respectively.

The velocity jump across the vortex sheet is (cf. (2.24))

$$\gamma = \mathcal{J} T^{(2k-1)/3} \left|\frac{\mathrm{d}Z}{\mathrm{d}\lambda}\right|^{-1}, \tag{2.36}$$

which is always finite because $(2k-1)/3 = l \geqslant 0$, i.e. $k \geqslant 1/2$.

In summary, the three vortex types originally reported by PS21 constitute all possible vortex types generated at a sharp and straight edge of a solid body, provided (2.5) holds. A key implication is that starting vortices in many seemingly different configurations are controlled by the same physical mechanisms. This finding is explored in the sections that follow.

3. Case studies and underlying physics

In this section, we demonstrate that the vortex types described in § 2 apply to a wide range of flow problems. A focus is on the equivalences between the vortex sheet dynamics in several distinct examples, which can be discerned through the functions $f(T)$ and $g(T)$ that completely describe the flow physics.

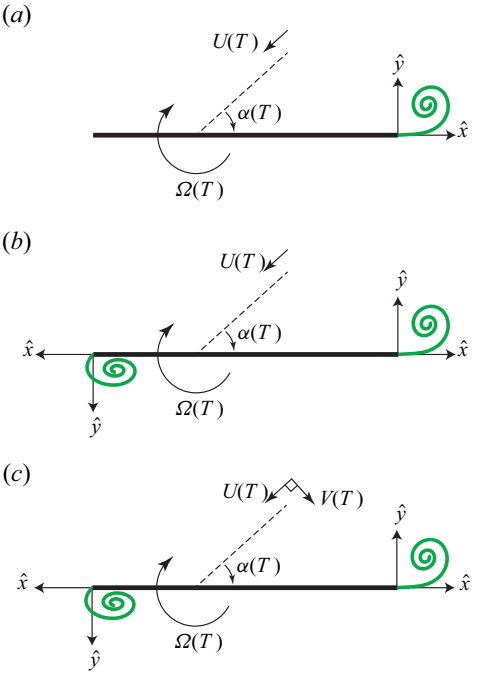

Figure 2. Starting vortices generated by a flat plate that is translating with velocity, $U(T)$, in a fixed direction in the laboratory frame, with an instantaneous angle of attack, $\alpha(T)$, and an instantaneous angular velocity, $\Omega(T)$, about a pivot point in the plane of the plate. (*a*) Trailing-edge vortex as studied by PS21; see § 3.1. (*b*) Leading- and trailing-edge vortices of the same plate motion; see § 3.2. (*c*) Leading- and trailing-edge vortices when the plate has an additional translational velocity component, $V(T)$, perpendicular to $U(T)$; see § 3.3.

3.1. *Trailing-edge vortex of a translating and rotating flat plate*

We first demonstrate application of the general theory reported in § 2 to the sudden translation and rotation of a flat plate in an unbounded and quiescent fluid (PS21); see figure 2(*a*). The required conformal mapping of the flat plate in z-space to the unit circle in ζ-space is given in (2.3*c*) of PS21.

The plate is of length, $2a$, and a global $(\tilde{x}, \tilde{y})$-Cartesian frame is referenced to the moving plate, which is aligned along $\tilde{y} = 0$ and occupies the region, $-a(1+d) \leqslant \tilde{x} \leqslant a(1-d)$. Note that this global frame differs from the (x, y)-Cartesian frame local to each edge; see § 2.1. The rotation pivot position is (i) at the origin of the $(\tilde{x}, \tilde{y})$-frame, and (ii) displaced a (signed) distance of ad from the plate centre. For example, $d = 1/2$ corresponds to a rotation pivot position at a distance of $a/2$ to the right of the plate centre in figure 2, which is the three-quarter-chord position; whereas $d = -1/2$ is the quarter-chord position. The plate moves with the (dimensionless) translational speed, $U(T) = T^m$, and rotates with the (dimensionless) angular velocity $\Omega(T) = \beta T^p$, where $m, p \geqslant 0$ and β is a real-valued constant. The instantaneous angle of attack of the plate is $\alpha(T) = \alpha_0 + \beta T^{1+p}/(1+p)$, where α_0 is a real-valued constant. We have used the length scale $\mathcal{L} = a$ and timescale $\mathcal{T} = a/U_0$ for a characteristic translational velocity of U_0. In summary, we have

$$U(T) = T^m, \quad \Omega(T) = \beta T^p, \quad \alpha(T) = \alpha_0 + \frac{\beta}{1+p} T^{1+p}. \tag{3.1a–c}$$

The velocity field of the attached flow, local to the trailing edge, is ((2.9) of PS21)

$$u_a - \mathrm{i}v_a = -\frac{\mathrm{i}}{\sqrt{2}}\hat{z}^{-1/2}\left(\left[\frac{1}{2}-d\right]\Omega + U\sin\alpha\right) + U\cos\alpha + o(1), \tag{3.2}$$

which aligns with the assumed form in (2.5), giving

$$f(T) = -\frac{\mathrm{i}}{\sqrt{2}}\left(\left[\frac{1}{2}-d\right]\Omega + U\sin\alpha\right), \quad g(T) = U\cos\alpha. \tag{3.3a,b}$$

Note that (2.4) of PS21 separates out a rigid-body-rotation term in the complex potential, W_a, and thus differs from the present definition in (2.4). This difference does not affect the overall velocity field, which is the transport quantity of primary interest in the present general theory; see above and (2.9) of PS21.

All results reported by PS21 can be recovered using the general theory in § 2 with (3.3*a*,*b*). For example, in the case that $\alpha_0 = 0$ and $d \neq 1/2$, we find

$$k = p, \quad l = m, \quad f_0 = -\frac{\hat{\beta}}{\sqrt{2}}, \quad g_0 = 1, \tag{3.4a–d}$$

where

$$\hat{\beta} = \beta\left(\tfrac{1}{2} - d\right). \tag{3.5}$$

3.1.1. *Vanishing plate rotation and degenerate vortex sheets*

We now clarify a feature of this flow reported in § 5.6 of PS21. For non-zero initial angle of attack, $\alpha_0 \neq 0$, this previous study showed that the starting vortex for $\beta \to 0^+$ can differ from identically zero rotation, $\beta = 0$ (which was studied by Pullin (1978)). It was suggested that this difference might be resolved by the inclusion of viscosity. Here, we show that it is a natural consequence of inviscid flow dynamics alone.

Importantly, PS21 took $T \to 0$ before $\beta \to 0^+$, whereas Pullin (1978) set $\beta = 0$ (no rotation) and then took $T \to 0$. These are complementary, but fundamentally different, limits were reported to produce different results:

(i) ($m = 1, p < 1, d \neq 1/2$): Type-I vortices with different growth rates in time, which for non-zero rotation $\beta > 0$, depend on the time power law of angular rotation, p; and

(ii) ($m = 0, p \geqslant 0$): Identical type-I vortices that are independent of p.

This behaviour is now explored through the form of $f(T)$ from the general theory in § 2, and is relevant to understanding the evolution of the starting vortex.

For non-zero initial angle of attack, $\alpha_0 \neq 0$, the vortex dynamics are dominated by $f(T)$; see (2.11*a*,*b*), (2.18) and (3.3*a*,*b*). From (3.3*a*,*b*), it then follows that the vortex dynamics depend on the plate rotation if and only if

$$O\left(T^m|\sin\alpha_0|\right) < O\left(T^p\hat{\beta}\right) \quad \text{and} \quad d \neq 1/2. \tag{3.6a,b}$$

We explore finding (i) in detail.

For $m = 1$ and $p < 1$, i.e. $m > p$, we observe that (3.6*a*,*b*) is satisfied for small time, i.e. the vortex dynamics will depend on plate rotation. Rewriting (3.6*a*,*b*) as

$$T^{m-p} \ll \frac{\hat{\beta}}{|\sin\alpha_0|}, \tag{3.7}$$

and choosing a multiplicative factor, $\delta \ll 1$ for this inequality to hold, gives the upper bound in time,

$$T < T_{max} \equiv \left| \frac{\delta\hat{\beta}}{\sin\alpha_0} \right|^{1/(m-p)}, \tag{3.8}$$

for which plate rotation affects the vortex dynamics.

This shows that as $\hat{\beta} \to 0^+$, a type-I vortex depending on plate rotation arises at $T = 0^+$ which quickly (immediately) morphs into a vortex whose dynamics are independent of plate rotation and coincide with Pullin (1978). That is, a boundary layer in time exists. This boundary layer is independent of viscosity and can, in principle, be discerned from the present inviscid formulation using the time scale in (3.7).

The above analysis is straightforward to adapt to other settings. Explanation of finding (ii) for the complementary case of $m \leqslant p$ is provided in PS21, is not in contention and, hence, omitted here. The difference in dynamics for $m \geqslant p$ and $m < p$, including the above-described vortex morphing, should be observable in experiment.

3.2. *Starting vortex at the leading edge of a translating and rotating flat plate*

Next, we examine the starting vortex at the leading edge of the same plate as § 3.1; as per the illustrated left-hand vortex in figure 2(*b*). This starting vortex configuration has not been reported previously.

By considering a Cartesian frame local to the leading edge of the plate, as shown in figure 2(*b*), and expanding the attached flow in (2.4) of PS21 about this leading edge, we obtain

$$u_a - \mathrm{i}v_a = -\frac{\mathrm{i}}{\sqrt{2}}\hat{z}^{-1/2}\left(\left[\frac{1}{2}+d\right]\Omega - U\sin\alpha\right) - U\cos\alpha + o(1), \tag{3.9}$$

which upon comparison with the canonical form in (2.5), gives

$$f(T) = -\frac{\mathrm{i}}{\sqrt{2}}\left(\left[\frac{1}{2}+d\right]\Omega - U\sin\alpha\right), \quad g(T) = -U\cos\alpha. \tag{3.10a,b}$$

Using the power-law-in-time motion described in § 3.1, these become

$$f(T) = -\frac{\mathrm{i}}{\sqrt{2}}\left[\tilde{\beta}\,T^p - T^m\sin\alpha(T)\right], \quad g(T) = -T^m\cos\alpha(T), \tag{3.11a,b}$$

where

$$\tilde{\beta} \equiv \beta\left(\tfrac{1}{2}+d\right). \tag{3.12}$$

The form of $g(T)$ in (3.10*a*,*b*) gives $g_0 < 0$. This establishes that a type-II vortex described in § 2.4.2 cannot exist at the leading edge of the plate; the vortex sheet would lie along the plate itself, which is not allowed.

As an example, we consider the special case of $\alpha_0 = 0$ and $d \neq -1/2$, for which the general theory in § 2 yields

$$k = p, \quad l = m, \quad f_0 = -\frac{\tilde{\beta}}{\sqrt{2}}, \quad g_0 = -1. \tag{3.13a–d}$$

Substituting (3.13*a–d*) into (2.23) for type-I vortices, and (2.35) for type III, gives the respective governing equations for these leading-edge vortices. Namely, for type I we obtain

$$\frac{2p+2}{3}\bar{Z} + \frac{4p+1}{3}(1-\lambda)\frac{\mathrm{d}\bar{Z}}{\mathrm{d}\lambda} = -\frac{\tilde{\beta}}{\sqrt{2}}\mathrm{i}\, Z^{-1/2}\,(1 + M(Z))\,, \tag{3.14}$$

whereas for type III we have

$$\frac{2p+2}{3}\bar{Z} + \frac{4p+1}{3}(1-\lambda)\frac{\mathrm{d}\bar{Z}}{\mathrm{d}\lambda} = -\frac{\tilde{\beta}}{\sqrt{2}}\mathrm{i}\, Z^{-1/2}\,(1 + M(Z)) - 1, \tag{3.15}$$

where the function $M(Z)$ is defined in (2.19). This example highlights the utility of the general theory in § 2, which facilitates calculation of the starting vortex at any straight edge of a solid body. All that is required are the constants, f_0 and g_0, which immediately follow from $f(T)$ and $g(T)$ in the attached flow local to the particular edge.

The special case of vanishing rotation furnishes the following expressions at the leading edge,

$$f_0 = \frac{\sin\alpha_0}{\sqrt{2}}, \quad g_0 = -\cos\alpha_0, \tag{3.16a,b}$$

with the corresponding results at the trailing edge given by a sign change in f_0 and g_0. At both edges, the dominant power law is $k = l = m$. For $0 < \alpha_0 < \pi/2$, the trailing- and leading-edge vortex sheets are both of type I, but have different shapes. For $\alpha_0 = 0$, there is no leading-edge vortex whereas the trailing-edge vortex sheet is of type II. For normal incidence, i.e. $\alpha_0 = \pi/2$, the vortex sheets are of type I and identical in shape, while being mirror images about the normal direction to the plate surface.

A summary of results for the leading-edge vortex sheets, and their respective regimes of validity, can be calculated in an identical manner to that performed in PS21 for the trailing-edge vortex. These results for the leading-edge vortex of a flat plate are summarised in table 1; see also the complementary table 1 of PS21.

Comparison of the results in table 1 of PS21 and table 1 establishes that the starting vortices at the trailing and leading edges for $\alpha_0 = 0$ can differ in type, provided that $d = \pm 1/2$, i.e. rotation occurs at either the quarter- or three-quarter-chord position of the plate. This is because the effect of plate rotation, i.e. $\Omega(T)$, on the perpendicular component of local flow, $f(T)$, vanishes at one of the plate edges but not the other; the term $\Omega(T)$ is multiplied by $1/2 - d$ and $1/2 + d$ for the trailing and leading edges, respectively. This feature is quantified in the phase diagram reported in figure 3 for $d = 1/2$. It shows the pairs of vortex types that arise at the leading and trailing edges, as a function of the plate translation and rotation power laws, m and p, respectively. Combinations of types I and II, I and III, and II and III are all possible.

This feature is now illustrated using three examples for zero initial angle of attack, $\alpha_0 = 0$, for which type-III vortices can arise. Integro-differential equations for the type-III vortex sheets are solved numerically using the method reported in § 5.1.2 of PS21. Results are given for translation and rotation power laws of $m = 1$ and $p = 2$, respectively, and a

Angle and pivot	Power laws	Type	Vortex, q	Vortex, s	Local attached flow component
$\alpha_0 = 0, d \neq -1/2$	$m > (2p-1)/3$	I	$2(1+p)/3$	$(1+4p)/3$	Perpendicular
	$m = (2p-1)/3$	III	$2(1+p)/3$	$(1+4p)/3$	Perpendicular and parallel
	$m < (2p-1)/3$	None	—	—	None
$\alpha_0 = 0, d = -1/2$	$m > 1+2p$	I	$2(2+m+p)/3$	$(5+4m+4p)/3$	Perpendicular
	$m = 1+2p$	III	$2(1+p)$	$3+4p$	Perpendicular and parallel
	$m < 1+2p$	None	—	—	None
$\alpha_0 \neq 0, d \neq -1/2$	$m > p$	I	$2(1+p)/3$	$(1+4p)/3$	Perpendicular
	$m = p, \tilde{\beta} \neq \sin\alpha_0$	I	$2(1+p)/3$	$(1+4p)/3$	Perpendicular
	$m = p, \tilde{\beta} = \sin\alpha_0$	None	—	—	None
	$m < p$	I	$2(1+m)/3$	$(4m+1)/3$	Perpendicular
$\alpha_0 \neq 0, d = -1/2$	All	I	$2(1+m)/3$	$(4m+1)/3$	Perpendicular

Table 1. Summary of vortex sheets arising from the leading edge of a flat plate. Results are given as a function of the plate translation and rotation parameters, defined in (3.1*a–c*) and (3.12). Time power laws, $q \geqslant 0$ and $s \geqslant 0$, of their similarity solutions are as defined in (4.1*a*,*b*) of PS21, with the local flow near the leading edge of the plate given in (3.9). This table complements table 1 of PS21 that reports results for the trailing-edge vortex. The dominant component of the local attached flow to the edge, that drives the vortex sheet, is indicated in the right-most column.

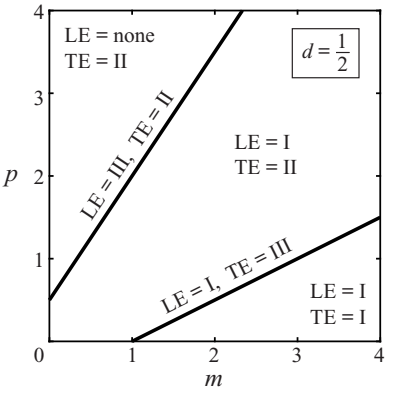

Figure 3. Phase diagram of the vortex sheet pairs that simultaneously arise at the leading edge (LE) and trailing edge (TE) of a flat plate, for $\alpha_0 = 0$ and rotation about the three-quarter-chord position, $d = 1/2$. Results are given as a function of the plate translation and rotation power-laws, m and p, respectively, defined in (3.1*a–c*). The data are derived from tables 1 of PS21 and table 1; an analogous phase diagram arises for rotation about the quarter-chord position.

dimensionless angular velocity, $\beta = \sqrt{2}$. These results highlight the effect of varying the rotation pivot position, d.

Example 3.1. Figure 4(*a*) gives the starting vortices generated at the edges of a flat plate that is undergoing translation and rotation about its centre, i.e. $d = 0$. Type-III vortices are generated at both edges; as per table 1 of PS21 and table 1. Despite the same vortex type, the shape of the vortices at the leading and trailing edges differ. The leading-edge

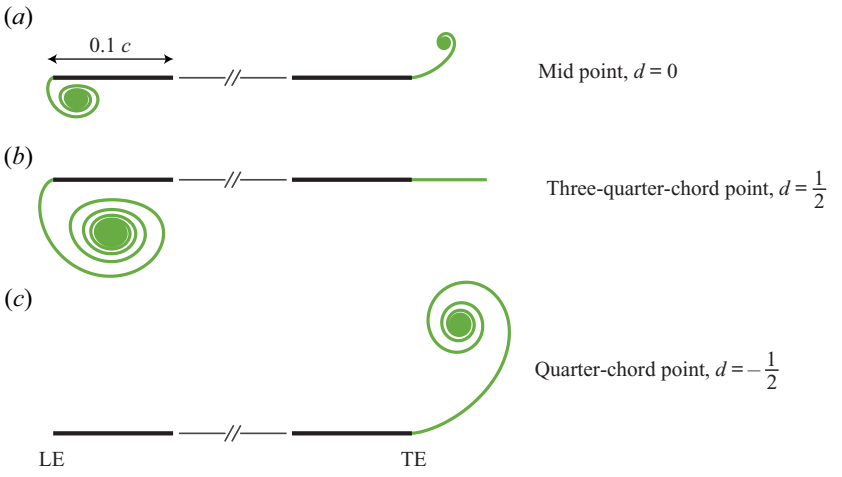

Figure 4. Leading- and trailing-edge vortices (green lines) generated by a flat plate (black lines) that is translating and rotating with time power laws, $m = 1$ and $p = 2$, respectively. A dimensionless angular velocity of $\beta = \sqrt{2}$ and a convective time of $T = 1/2$ are used. (*a*) Rotation about the plate centre, $d = 0$. (*b*) Rotation about the three-quarter-chord position, $d = 1/2$. (*c*) Rotation about the quarter-chord position, $d = -1/2$. The central region of the flat plate is not shown to accentuate the structure of the starting vortices at its edges; leading edges (LE) and trailing edges (TE) are indicated. The plate chord is $c = 2a$ and all plots are referenced to this scale as indicated in (*a*). Type-III vortex sheets computed using the numerical method reported in § 5.1.2 of PS21.

vortex is strongly affected by its proximity to the flat plate, rolling up as it approaches the flat plate, whereas the trailing-edge vortex is swept downstream and, thus, less affected. This difference in behaviour is generated mathematically by the sign change in g_0 for the trailing and leading edges, cf. (5.19) of PS21 and (3.15).

Example 3.2. The configuration used in example 3.1 is now altered to rotate the plate about the three-quarter-chord position, $d = 1/2$. Figure 3 shows that a type-III vortex is generated at the leading edge, whereas a type-II vortex arises at the trailing edge, with the following dominant terms in $f(T)$ and $g(T)$ (see (3.1*a–c*) and (3.3*a*,*b*)):

$$f(T) = -\frac{\mathrm{i}\, T^4}{3}, \quad g(T) = T, \tag{3.17a,b}$$

giving $f_0 = -1/3$, $g_0 = 1$, $l = 1$ and $k = 4$. The self-similar solution of the trailing-edge vortex sheet is given by (see (2.11*a*,*b*), (2.29) and (2.31)),

$$\hat{z}_v = T^2 Z(\lambda), \quad \lambda = 1 - \frac{\Gamma}{\mathcal{J}\, T^5}, \quad Z = \frac{1}{2}\left(1 - (1-\lambda)^{2/5}\right), \quad \mathcal{J} = \frac{16\sqrt{2}}{45}. \tag{3.18a–d}$$

These vortices are shown in figure 4(*b*) and highlight the difference in dynamics that can occur by simply changing the plate rotation position. Note that the starting vortices are self-similar in time, T, and thus no extra information is discerned by changing the time. Changing the dimensionless angular velocity, β, alters the shape of the type-III leading-edge vortex, whereas the type-II vortex remains unchanged at the trailing edge; as per the nature of these different vortices (data not shown).

Example 3.3. Finally, the plate pivot position is moved to the quarter-chord position, $d = -1/2$. Table 1 of PS21 and table 1 then show that no vortex is generated at the

leading edge, whereas the trailing-edge vortex is of type III. Figure 4(*c*) shows the resulting vortex flow, which differs considerably from plate rotation about its centre and the three-quarter-chord position.

3.2.1. *Aerofoil design of model aeroplanes and other low-speed aircraft*

The findings of example 3 are relevant to the design of model aeroplanes (Schmitz 1941) and other low-speed aircraft, including MAVs and UAVs (Winslow *et al.* 2018). The aerofoils of these aircraft operate at Reynolds numbers much lower than those of conventional planes, which can lead to laminar separation near the aerofoil's leading edge. Consequently, these aircraft often use thin aerofoils with low curvature, e.g. flat plates, that induce a separation bubble near the aerofoil's sharp leading edge with an attached turbulent boundary layer downstream. This gives these aerofoils their characteristic high lift-to-drag ratio. Importantly, the quarter-chord position of these aerofoils is the aerodynamic centre, i.e. the position where the pitching moment is independent of the angle of attack.

The present analysis now shows that choice of this position, i.e. $d = -1/2$, can completely suppress the starting vortex at the leading (sharp) edge, whilst generating a type-III vortex at the trailing edge. The shape of the trailing-edge vortex, which now defines the total lift the wing experiences at start up, can then be tuned by adjusting β, i.e. the relative magnitude of angular and translational speeds of the aerofoil.

That is, leading-edge separation is suppressed at start up if the aeroplane translates with constant acceleration ($m = 1$) and the angular acceleration of its aerofoil increases linearly with time ($p = 2$). For more general power laws, i.e. aerofoil translation/rotation, leading-edge vortex suppression at zero initial angle of attack, $\alpha_0 = 0$, occurs when $m < 1 + 2p$ for rotation about the aerodynamic centre, $d = -1/2$; see table 1. This condition applies under a wide range of practically relevant conditions. As an example, for constant translational acceleration, $m = 1$, the leading-edge vortex is always suppressed unless the angular velocity power law $p = 0$, i.e. (abrupt) impulsive rotation.

This finding is relevant to the take-off dynamics of model aeroplanes and other low-speed aircraft, whose motion normally starts from rest with smooth rotation of the wing.

3.3. *Three independent components of the plate motion*

We now address an important and unresolved question: which velocity components of a flat plate independently control its starting vortices?

To achieve this goal, we generalise the problem studied by PS21 to include a translational velocity component, $V(T)$, that acts perpendicular to $U(T)$; see figure 2(*c*). The velocity field local to the trailing edge becomes

$$u_a - \mathrm{i}v_a = -\frac{\mathrm{i}}{\sqrt{2}}\,\hat{z}^{-1/2}\left(\left[\frac{1}{2} - d\right]\Omega + U\sin\alpha + V\cos\alpha\right) + U\cos\alpha - V\sin\alpha + o(1). \tag{3.19}$$

The functions, f and g, then take the form,

$$f(T) = -\frac{\mathrm{i}}{\sqrt{2}}\left(\left[\frac{1}{2} - d\right]\Omega + U\sin\alpha + V\cos\alpha\right), \quad g(T) = U\cos\alpha - V\sin\alpha, \tag{3.20a,b}$$

which reduce to the canonical forms in (3.3*a*,*b*) (with only one translational velocity component) by defining

$$\hat{U}(T) = \sqrt{U^2 + V^2}, \quad \hat{\alpha}(T) = \alpha + \tan^{-1}\left(\frac{V}{U}\right). \tag{3.21a,b}$$

This finding proves that there are only two independent components of the plate motion that control the trailing-edge starting vortex. An identical finding holds for the leading-edge vortex by virtue of § 3.2. Consequently, the analysis of PS21 together with the results of § 3.2 encompass the general case, including the starting vortices generated by a plate undergoing pure translational motion. The corollary is that pure translational motion of the plate edge can and does recover the starting vortices reported by PS21, without any plate rotation.

As an example, consider the special case of pure rotation about the plate's trailing edge, i.e. $U = V = 0$ and $d = 1$. The functions defined in (3.20*a*,*b*) become

$$f(T) = \frac{\mathrm{i}}{2^{3/2}}\Omega(T), \quad g(T) = 0, \tag{3.22a,b}$$

where $\Omega(T) = \beta T^p$, and so a type-I vortex sheet arises. The starting dynamics of this vortex can be identically reproduced by pure translation of the edge, with $\alpha_0 = -\pi/2$, $U = \beta T^p/2$ and $V = 0$, i.e. the plate edge translates normal to its axis.

Together with the above analysis, this establishes that (i) pure translation of an edge or (ii) a combination of translation and rotation of the same edge, are locally equivalent with respect to the starting vortex, and can be mapped onto each other.

This finding pertains only to the flow local to any particular edge. Namely, the (local) starting vortex generated at a single edge of a translating and rotating solid body can always be reproduced by pure translation of the same edge with two velocity components. However, these two velocity components can vary across the different edges of a solid body. This was highlighted in § 3.2, where we showed that the vortices generated at the edges of a flat plate can differ in type, which cannot be reproduced by pure translational motion of the same flat plate. This establishes a fundamental distinction between equivalent local motion of an edge and global motion of the solid body.

3.4. *Relationship between Cortelezzi & Leonard (1993) and PS21*

Equation (3.20*a*,*b*) and the discussion in the previous section now establish that the starting vortex problems studied by Cortelezzi & Leonard (1993) and PS21, while seemingly different, are in fact related. Cortelezzi & Leonard (1993) studied vortex generation by the edge of a semi-infinite plate moving in its plane, with an imposed normal flow. PS21 calculated the trailing-edge vortices of a finite plate undergoing simultaneous translation and rotation.

To make the equivalence between these apparently different studies transparent, we examine the structure of the attached flow local to the plate edge in Cortelezzi & Leonard (1993). The semi-infinite plate studied by Cortelezzi & Leonard (1993) lies along the negative y-axis, its Cartesian frame is fixed to the plate with the impinging flow in the x-direction; its origin is at the edge. In the notation of Cortelezzi & Leonard (1993), the fluid moves relative to the plate with velocity components, $U_f(T)$ and $-u_p(T)$, in the directions perpendicular and parallel to the plate, respectively. Note that the symbol, U, appears in (2) of Cortelezzi & Leonard (1993), which is replaced by U_f here to avoid confusion with the definition in (3.1*a*–*c*). As per § 2, we orient the x-direction parallel to the plate edge: accordingly, we rotate the Cartesian frame used in Cortelezzi & Leonard

(1993) by $\pi/2$. The velocity field for the attached flow is then (see (2) of Cortelezzi & Leonard 1993)

$$u_a - \mathrm{i}v_a = \frac{\mathrm{i}}{2}U_f(T)\hat{z}^{-1/2} - u_p(T), \tag{3.23}$$

with

$$U_f(T) = -\mathcal{V}T^m, \quad u_p(T) = -T^n, \tag{3.24a,b}$$

where m and n are power laws as per Cortelezzi & Leonard (1993) and $\mathcal{V}$ has been scaled such that it is the ratio of the (dimensional) characteristic velocity perpendicular and parallel to the plate. From (3.24*a*,*b*), it follows that the canonical functions, f and g, defined in (2.5) take the form

$$f(T) = -\frac{\mathrm{i}}{2}\mathcal{V}T^m, \quad g(T) = T^n, \tag{3.25a,b}$$

and, hence, (2.11*a*,*b*) gives

$$f_0 = -\tfrac{1}{2}\mathcal{V}, \quad g_0 = 1. \tag{3.26a,b}$$

These results together with those provided in (3.3*a*,*b*) (of identical form) define the mapping between the starting vortices studied by Cortelezzi & Leonard (1993) and PS21:

$$(m, p)_{PS} \mapsto (n, m)_{CL}, \quad \hat{\beta}_{PS} \mapsto \tfrac{1}{\sqrt{2}}\mathcal{V}_{CL}, \tag{3.27a,b}$$

where the subscripts *PS* and *CL* refer to symbols used in PS21 and Cortelezzi & Leonard (1993), respectively.

For example, the critical line for type-III vortices reported by PS21 in the case that $\alpha_0 = 0$ and $d \neq 1/2$, is

$$m = \tfrac{1}{3}(2p - 1), \tag{3.28}$$

whereas the critical line reported by Cortelezzi & Leonard (1993) is

$$3(n + 1) - 2(m + 1) = 0. \tag{3.29}$$

Equation (3.29) is identical to (3.28) under the mapping defined in (3.27*a*,*b*).

The attached flow components, $f(T) \sim U_f(T)$ and $g(T) \sim u_p(T)$, are associated with flow perpendicular and parallel to the straight edge, respectively (Cortelezzi & Leonard 1993). A type-I vortex arises when $f(T)$ dominates, whereas a type-II vortex occurs when $g(T)$ dominates; a type-III vortex exists when they are in balance.

3.5. *Joukowski aerofoil*

Finally, we examine a solid body that differs from the flat plate considered in the previous sections and in the majority of literature reports on the starting vortex. A Joukowski aerofoil is defined in the z-plane by

$$z = \frac{1}{2}\left(\zeta - 1 + \frac{\mathrm{e}^{2\mathrm{i}\gamma}}{\zeta - 1 + \mathrm{e}^{\mathrm{i}\gamma}} - \mathrm{e}^{\mathrm{i}\gamma}\right)\mathrm{e}^{\mathrm{i}\gamma}, \quad \zeta = 1 - R + R\mathrm{e}^{\mathrm{i}\theta}, \tag{3.30a,b}$$

where $\gamma \in [-\pi, \pi)$ defines the camber of the aerofoil in the z-plane, R is the radius of a circle centred at $\zeta = 1 - R$ in the (conformally mapped) ζ-plane defining the thickness of the aerofoil, and $\theta \in [-\pi, \pi)$ is the polar angle to the real axis of the ζ-plane that parametrises the circle; see figure 5. The trailing edge of the aerofoil is positioned at $z = 0$

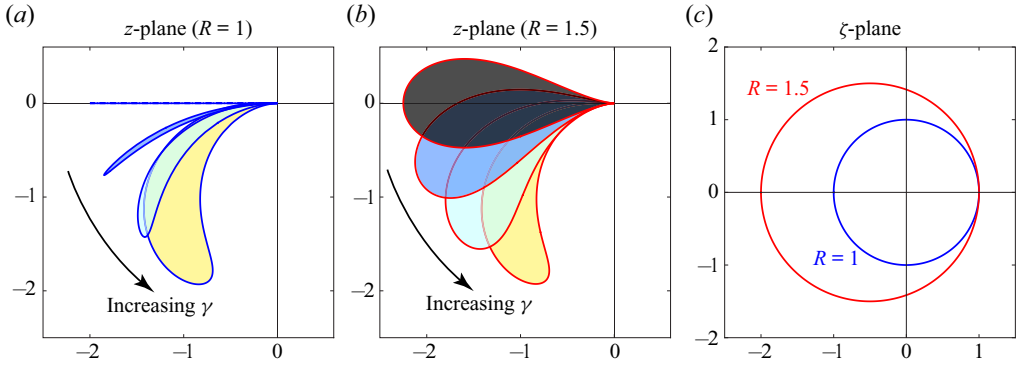

Figure 5. Sample Joukowski aerofoils under the mapping (3.30*a*,*b*). Aerofoils in the physical z-plane with different thickness parameter, $R = 1$ and 1.5, for increasing camber parameter, $\gamma = n\pi/16$, where $n = 0, 1, 2, 3$. Corresponding circles in the (conformally mapped) ζ-plane are also illustrated.

and is parallel to the real (horizontal) axis of the z-plane; see figure 5. The aerofoil is stationary in the z-plane.

The symmetric Joukowski aerofoil, i.e. $\gamma = 0$, has its leading edge at

$$z = -\frac{2R^2}{2R-1}, \tag{3.31}$$

giving a dimensionless chord length, ℓ, of

$$\ell = \frac{2R^2}{2R-1}. \tag{3.32}$$

Equation (3.32) recovers the dimensionless chord length of the flat plate considered in § 3.1, i.e. $\ell = 2$ when $R = 1$ and $\gamma = 0$; see figure 5. Thus, results for the symmetric Joukowski aerofoil in this section can be systematically compared to those for the flat plate in § 3.1, as R is varied from unity.

For an imposed uniform flow of (i) velocity, $U(T)$, at fixed angle of attack, α_0, to the real axis of the z-plane, and (ii) velocity, $V(T)$, perpendicular to the direction of $U(T)$, the complex potential of the attached flow generated by the aerofoil in the ζ-plane is (Batchelor 1967)

$$W_a = \frac{1}{2}\left((U - \mathrm{i}V)(\zeta - 1 + R)\exp(\mathrm{i}(\gamma - \alpha_0)) + (U + \mathrm{i}V)\frac{R^2\exp(\mathrm{i}(\alpha_0 - \gamma))}{\zeta - 1 + R}\right), \tag{3.33}$$

whose corresponding velocity field is $u_a - \mathrm{i}v_a \equiv \partial W_a/\partial z$. Note that the 'effective' angle of attack is $\alpha_0 - \gamma$, as required (Batchelor 1967, chap. 6.7).

We consider the trailing edge of the aerofoil (at $z = 0$), and expand its attached velocity field locally to this edge; the characteristic length scale for the flow is taken to be unity,

i.e. $\mathcal{L} = 1$. This gives

$$u_a - \mathrm{i}v_a = -\frac{\mathrm{i}}{\sqrt{2}}\hat{z}^{-1/2}\left(U\sin(\alpha_0-\gamma) + V\cos(\alpha_0-\gamma)\right) + \frac{U}{2}\left(\exp(-\mathrm{i}\alpha_0) - \exp(\mathrm{i}(\alpha_0-2\gamma)) + \frac{2}{R}\exp(\mathrm{i}(\alpha_0-\gamma))\right) + \frac{\mathrm{i}V}{2}\left(-\exp(-\mathrm{i}\alpha_0) - \exp(\mathrm{i}(\alpha_0-2\gamma)) + \frac{2}{R}\exp(\mathrm{i}(\alpha_0-\gamma))\right) + \text{higher order}, \tag{3.34}$$

which, as required, reduces to the attached flow past a flat plate when $R = 1$ and $\gamma = 0$. Equations (2.5) and (3.34) then give

$$f(T) = -\frac{\mathrm{i}}{2^{1/2}}\left(U\sin(\alpha_0-\gamma) + V\cos(\alpha_0-\gamma)\right), \tag{3.35a}$$

$$g(T) = \frac{U}{2}\left(\exp(-\mathrm{i}\alpha_0) - \exp(\mathrm{i}(\alpha_0-2\gamma)) + \frac{2}{R}\exp(\mathrm{i}(\alpha_0-\gamma))\right) + \frac{\mathrm{i}V}{2}\left(-\exp(-\mathrm{i}\alpha_0) - \exp(\mathrm{i}(\alpha_0-2\gamma)) + \frac{2}{R}\exp(\mathrm{i}(\alpha_0-\gamma))\right). \tag{3.35b}$$

As before, the imposed flow follows independent power laws in time,

$$U = \mathcal{V}T^m, \quad V = \mathcal{W}T^n, \tag{3.36a,b}$$

where $\mathcal{V}$ and $\mathcal{W}$ are any real constants and the constant power laws, $m, n \geqslant 0$.

When $\alpha_0 - \gamma \neq 0, \pi/2, \pi$, the $f(T)$ term always dominates $g(T)$ in the governing Birkhoff–Rott equation and its associated Kutta condition, i.e. a type-I vortex arises. This case is associated with the dominance of perpendicular flow at the trailing edge. The dominant contribution to $f(T)$, as defined in (2.11*a*,*b*), then follows

$$f_0 = -\frac{1}{\sqrt{2}}\begin{cases}\mathcal{V}\sin(\alpha_0-\gamma), & m<n\\ \mathcal{W}\cos(\alpha_0-\gamma), & m>n\\ \mathcal{V}\sin(\alpha_0-\gamma)+\mathcal{W}\cos(\alpha_0-\gamma), & m=n\end{cases}, \quad k = \begin{cases} m, & m<n\\ n, & m>n\\ m, & m=n\end{cases}. \tag{3.37a,b}$$

For the special case of $\alpha_0 = \gamma$, it is possible for a type-II or type-III vortex sheet to arise because the parallel component of flow at the trailing edge can be dominant. For this case, (3.37*a*,*b*) gives

$$f_0 = -\frac{\mathcal{W}}{\sqrt{2}}, \quad k = n, \tag{3.38a,b}$$

whereas (3.35*b*) reduces to

$$g(T) = \frac{\mathcal{V}T^m}{R} + \frac{\mathrm{i}\mathcal{W}T^n}{R}\left(1 - R\exp(-\mathrm{i}\alpha_0)\right). \tag{3.39}$$

It is evident from the forms of these equations that the trailing-edge vortex exhibits identical types to those of the flat plate with zero initial angle of attack, as the power laws m and n are varied. The similarity solution for the trailing-edge vortex of the Joukowski aerofoil easily follows from the general formulae in § 2; this is left as an exercise for the reader.

Next, we consider three example vortex sheets generated at the trailing edge of a Joukowski aerofoil.

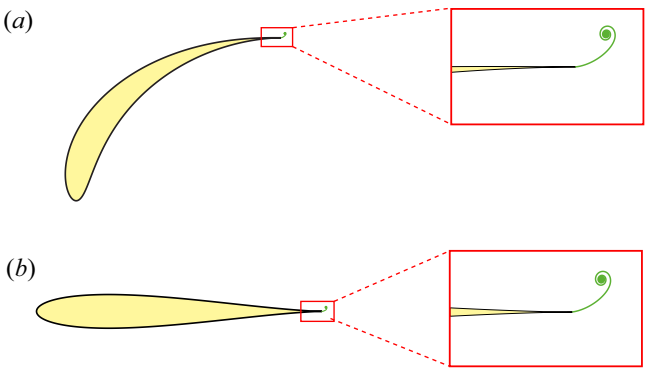

Figure 6. Type-III vortex sheet for $T = 1/2$ (green) at the trailing edge of (*a*) a cambered Joukowski aerofoil (case B; § 3.5.2), and (*b*) a symmetric Joukowski aerofoil (case C; § 3.5.3). The images on the right provide an enlarged-view version of the trailing edge, highlighting the shape of the vortex sheet. The vortex sheets in (*a*,*b*) are identical to that at the trailing edge of the flat plate in figure 4(*a*).

3.5.1. *Case A: symmetric Joukowski aerofoil with type-II vortex sheet*

First, consider a symmetric Joukowski aerofoil with initial angle of attack, $\alpha_0 = 0$, camber parameter, $\gamma = 0$, thickness parameter, $R \geqslant 1$. The power laws in (3.36*a*,*b*) are set to $m = 0$ and $n = 2$, i.e. impulsive start-up in the direction parallel to the plate with a smooth (and slower) acceleration in the perpendicular direction. A type-II vortex sheet arises with

$$k = n = 2, \quad l = m = 0, \quad g_0 = \frac{\mathcal{V}}{R}, \tag{3.40a–c}$$

and f_0 is given by (3.38*a*,*b*). The vortex sheet has the self-similar solution,

$$\hat{z}_v = T\frac{\mathcal{V}}{R}\left(1 - (1-\lambda)^{2/5}\right), \quad \mathcal{J} = \frac{16}{15}\mathcal{W}\sqrt{\frac{2\mathcal{V}}{R}}, \tag{3.41a,b}$$

with a dimensionless length of $\mathcal{V}T/R$, which is inversely proportional to the aerofoil's thickness parameter, R. That is, a thicker symmetric Joukowski aerofoil produces a shorter trailing-edge vortex. Equation (2.33) gives the corresponding velocity jump across the vortex sheet,

$$\gamma = \frac{8}{3}\sqrt{\frac{2R}{\mathcal{V}}}T^{3/2}\left(1 - \frac{R\hat{x}_v}{\mathcal{V}T}\right)^{3/2}, \tag{3.42}$$

whereas the total circulation follows from (2.13) and (2.26*a*,*b*), and is $\Gamma_0(T) = \mathcal{J}T^{5/2}$.

3.5.2. *Case B: cambered Joukowski aerofoil with type-III vortex sheet*

Second, we study an asymmetric (cambered) Joukowski aerofoil with initial angle of attack, $\alpha_0 = -3\pi/8$, camber parameter, $\gamma = \pi/8$, and thickness parameter, $R = 1$; see figure 5(*a*). The power laws in (3.36*a*,*b*) are set to $m = 2$ and $n = 1$, with velocity constants, $\mathcal{V} = -1/\sqrt{2}$ and $\mathcal{W} = 1$. A type-III vortex sheet is generated at the trailing edge, with

$$k = m = 2, \quad l = n = 1, \quad f_0 = -\tfrac{1}{2}, \quad g_0 = 1, \tag{3.43a–d}$$

which is shown in figure 6(*a*) for $T = 1/2$. This vortex sheet is identical to that generated at the trailing edge of the rotating and translating flat plate in figure 4(*a*).

3.5.3. *Case C: symmetric Joukowski aerofoil with type-III vortex sheet*

Third, we analyse a symmetric Joukowski aerofoil with $\alpha_0 = 0$, $\gamma = 0$ and $R = 11/10$. The power laws in (3.36*a*,*b*) are now set to $m = 1$ and $n = 2$, with velocity constants, $\mathcal{V} = R$ and $\mathcal{W} = -1/\sqrt{2}$. Again, a type-III vortex sheet arises at the trailing edge with

$$k = n = 2, \quad l = m = 1, \quad f_0 = -\tfrac{1}{2}, \quad g_0 = 1, \tag{3.44a–d}$$

which is illustrated in figure 6(*b*), again for $T = 1/2$. The parameters in this third case have been chosen such that the vortex sheet is identical to case B above, despite the different aerofoil geometry. This highlights a principal finding of this study that the vortex sheet is controlled by the flow local to the edge only, which is reflected in identical values for f_0 and g_0 in (3.43*a–d*) and (3.43*a–d*).

A vortex sheet identical to figure 6(*b*) is obtained under the mapping, $\mathcal{V} \to -\mathcal{W}$, $\mathcal{W} \to \mathcal{V}$, $m \leftrightarrow n$ and $\alpha_0 \to \alpha_0 + \pi/2$, because this produces the same attached flow. This mapping then gives values for m and n that coincide with case B.

4. Aerodynamic force experienced by a flat plate

A Bernoulli equation can be derived for unsteady rotation of a flat plate; see Appendix A.1. The aerodynamic force per unit length (i.e. per unit plate span, normal to the xy-plane) experienced by the plate then becomes (Appendix A.2 and Pullin & Wang 2004)

$$F_y - \mathrm{i}F_x = -\frac{\rho\mathcal{L}^3}{\mathcal{T}^2}\frac{\mathrm{d}}{\mathrm{d}T}\oint_{\mathcal{C}(T)} W(z,t)\,\mathrm{d}z, \tag{4.1}$$

where W is the (dimensionless) velocity potential and ρ is the fluid density. The contour, $\mathcal{C}(T)$, encloses and is adjacent to the flat plate and all vortex sheets generated at its edges. The integration contour, $\mathcal{C}(T)$, differs to that used in the Blasius theorem which is restricted to the body's surface only (Batchelor 1967).

The dimensionless velocity potential associated with a single vortex sheet is

$$W_v = -\frac{1}{2\pi\mathrm{i}}\int_{\Gamma_0(T)}^{0}\left(\log\left(\zeta_v - \zeta_v'\right) - \log\left(\zeta_v - \frac{1}{\bar{\zeta}_v'}\right)\right)\mathrm{d}\Gamma', \tag{4.2}$$

where $\Gamma_0(T)$ is the total circulation shed by the vortex sheet at time, T. The force exerted on the plate by this vortex is then (Pullin & Wang 2004)

$$F_y^{(v)} - \mathrm{i}F_x^{(v)} = -\frac{\rho\mathcal{L}^3}{\mathcal{T}^2}K\frac{\mathrm{d}}{\mathrm{d}T}\int_0^{\Gamma_0(T)}\left(\frac{1}{\bar{\zeta}_v'} - \zeta_v'\right)\mathrm{d}\Gamma', \tag{4.3}$$

where the superscript, (v), refers to the force arising from the vortex sheet, and $K = \lim_{\zeta\to\infty}\mathrm{d}z/\mathrm{d}\zeta$, which is a constant. Using the expansion in (2.2), the leading-order force takes the form

$$F_y^{(v)} - \mathrm{i}F_x^{(v)} = \frac{\rho\mathcal{L}^3}{\mathcal{T}^2}Kc_{1/2}\frac{\mathrm{d}}{\mathrm{d}T}\int_0^{\Gamma_0(T)}\left(\bar{z}_v'^{\,1/2} + \hat{z}_v'^{\,1/2}\right)\mathrm{d}\,\Gamma'. \tag{4.4}$$

This can be expressed in terms of the similarity solution for the vortex sheet using (2.12*a*,*b*), giving

$$F_y^{(v)} - \mathrm{i}F_x^{(v)} = \frac{\rho\mathcal{L}^3}{\mathcal{T}^2}Kc_{1/2}\mathcal{J}\left(s + \frac{q}{2}\right)T^{s+q/2-1}\int_0^1\left(\bar{Z}'^{1/2} + Z'^{1/2}\right)\mathrm{d}\lambda', \tag{4.5}$$

which applies to any vortex sheet, regardless of its type.

4.1. *Force generated by a type-II vortex sheet*

The aerodynamic force generated by a type-II vortex is now calculated analytically, using (4.5). Substituting (2.29) and (2.31) into (4.5) gives the general formula,

$$F_x^{(v)} = 0, \quad F_y^{(v)} = -\frac{2\pi\rho\mathcal{L}^3}{\mathcal{T}^2} K c_{1/2} f_0 g_0 T^{l+k}. \tag{4.6a,b}$$

As an example, we consider the trailing-edge vortex of a flat plate with $\alpha_0 = 0$ and $d \neq 1/2$, for which

$$K = 1, \quad c_{1/2} = \sqrt{2}, \quad k = p, \quad l = m, \quad f_0 = -\frac{\hat{\beta}}{\sqrt{2}}, \quad g_0 = 1, \tag{4.7a–f}$$

giving the required vortex-induced drag and lift forces,

$$F_x^{(v)} = 0, \quad F_y^{(v)} = \frac{2\pi\rho\mathcal{L}^3}{\mathcal{T}^2} \hat{\beta} T^{m+p}. \tag{4.8a,b}$$

This shows that, while a type-II vortex sheet is always parallel to the plate, the lift it generates is linearly proportional to the (rescaled) dimensionless angular velocity, $\hat{\beta}$, in the case that $d \neq 1/2$. It also depends on the sum of the translation and rotation power-laws, m and p.

This gives the lift force experienced by the flat plate wing explored in § 3.2.1, for $m = 1$, $p = 2$ and $d = -1/2$,

$$F_y^{(v)} = \frac{2\pi\rho\mathcal{L}^3}{\mathcal{T}^2} \beta T^3, \tag{4.9}$$

since $\hat{\beta} = \beta(1/2 - d)$. This cubic dependence of the lift force on time, T, and linear dependence on the angular velocity via β, should be observable in measurement for this experimentally realisable example.

4.2. *General formula for type-I vortex sheets at both edges of a flat plate*

As a further example of the utility of (4.5), we report general formulae for the lift force generated by type-I vortex sheets, that are shed from the edges of a flat plate. Cases for which $\alpha_0 = 0$ and $d \neq \pm 1/2$ are considered where identical vortex sheet types arise at both edges; see table 1 of PS21 and table 1. Note that the shape of these vortex sheets in the z-plane can only be evaluated numerically; for example, using the numerical method specified in § 5.1.2 of PS21.

Rescaling the Lagrangian coordinates of the vortex sheet and its shed circulation constant according to

$$Z = |f_0|^{2/3} \begin{cases} \omega, & f_0 > 0 \\ \bar{\omega}, & f_0 < 0 \end{cases}, \quad \mathcal{J} = \mathrm{sgn}(f_0)|f_0|^{4/3}\tilde{\mathcal{J}}, \tag{4.10a,b}$$

substituting (4.7a,b) and the corresponding expressions for the leading edge into (4.5), then gives the lift force experienced by the entire flat plate, arising from both vortex sheets,

i.e. at the leading and trailing edges,

$$F_Y^{(v)} = \frac{\rho \mathcal{L}^3}{2^{1/3}\mathcal{T}^2}\mathrm{sgn}(\beta)|\beta|^{5/3}\tilde{\mathcal{J}}\,(s+q/2)\,T^{s+q/2-1} \times \left(\mathrm{sgn}\left(\frac{1}{2}-d\right)\left|\frac{1}{2}-d\right|^{5/3} - \mathrm{sgn}\left(\frac{1}{2}+d\right)\left|\frac{1}{2}+d\right|^{5/3}\right)\int_0^1 \left(\bar{\omega}'^{1/2}+\omega'^{1/2}\right)\mathrm{d}\lambda', \tag{4.11}$$

where the subscript, Y, refers to the y-direction at the trailing edge. Note that the lift force vanishes for $d = 0$ because vortices with circulation of identical magnitude, but opposite sign, are generated at the leading and trailing edges.

An equivalent simplified formula for the lift experienced by the plate is not available for type-III vortices. This is because the vortex sheets at each edge exhibit different morphologies. Thus, the lift that each vortex sheet generates must be calculated separately (using (4.5)) and added together.

4.3. *Force experienced by a flat plate due to its attached flow*

In addition to the force generated by any shed vortex, a solid body experiences an additional force due to its attached flow; this is often referred to as an 'added apparent mass'. For a flat plate, this additional force is normal to the plate surface and is given by

$$F_X^{(a)} = 0, \quad F_Y^{(a)} = \frac{\pi\rho\mathcal{L}^3}{\mathcal{T}^2}\frac{\mathrm{d}}{\mathrm{d}T}\left(U\sin\alpha - \Omega\,\mathrm{d}\right), \tag{4.12a,b}$$

where we have used (4.1) together with (2.3) of PS21, the superscript, (a), refers to the force arising from the attached flow, with X and Y being the x and y-directions at the trailing edge of the plate, respectively.

5. Conclusions

We have reported a general theory that enables the starting vortices at all straight edges of a solid body to be calculated, i.e. surfaces adjacent to the edge are parallel. This generalises the recent work of PS21 who found that three vortex types can be generated at the trailing edge of a flat plate. We now show that these vortex types can appear at any straight edge of a solid body. The present theory is based on a canonical form for the attached flow at any particular edge, defined in (2.5), which depends on two functions, $f(T)$ and $g(T)$. The vortex dynamics at that particular edge follow directly from knowledge of these functions.

The physics of the starting vortex was then explored in several case studies.

(i) In § 3.1, we examined the trailing-edge vortex of a flat plate and clarified that the previously reported singular behaviour for pure translation, i.e. $\beta = 0$ and $\beta \to 0^+$ (PS21), arises from a purely inviscid process. Namely, a starting vortex of type I (that depends on rotation) initially forms but quickly for $\beta \ll 1$ (instantaneously for $\beta \to 0^+$) morphs into a vortex that is independent of plate rotation. Calculation of this transition is an area for future work.

(ii) In § 3.2, we calculated the leading-edge vortex of a flat plate using the general theory in § 2 and reported its results in table 1; complementing results in table 1 of PS21 for the trailing-edge vortex. This showed that different vortex types can arise at its leading and trailing edges when $d = \pm 1/2$.

(iii) One finding of significance is that the leading-edge vortex generated by a flat plate can be totally suppressed, for plate rotation about its aerodynamic centre, i.e. $d = -1/2$. This is true for a wide range of plate motions that depend on its translation and rotation: $m < 1 + 2p$. This is relevant to the aerofoil design of model aeroplanes and other low-speed aircraft, including MAVs and UAVs.

(iv) In § 3.3, we showed that combined translation/rotation of an edge (PS21) can be exactly mapped onto pure translation of the same edge, i.e. the vortex dynamics in both cases are equivalent.

(v) This enabled us to connect the seemingly unrelated works of Cortelezzi & Leonard (1993) and PS21 in § 3.4.

(vi) In § 3.5, the general theory was applied to the trailing-edge vortex of a Joukowski aerofoil, demonstrating the utility of the theory to solid bodies that differ from a flat plate.

(vii) With ability to calculate the overall dynamics of a solid body with any number of edges, we reported a general formula for the lift experienced by a flat plate in § 4.

Future work could determine the starting vortex dynamics for arrays of aerofoils, and even aerofoils with ground effect, given that analytical solutions for their attached flows have recently been reported (Baddoo & Ayton 2018; Baddoo *et al.* 2020). The present formulation could also be extended to edges of different angles, such as for flow past a wedge (Pullin 1978; Graham 1983).

Declaration of interests. The authors report no conflict of interest.

Author ORCIDs.
Edward M. Hinton https://orcid.org/0000-0002-2204-1204;
D.I. Pullin https://orcid.org/0009-0007-5991-2863;
John E. Sader https://orcid.org/0000-0002-7096-0627.

Appendix A. Aerodynamic force on a flat plate in the presence of rotation

In this appendix, we derive a general formula for the aerodynamic force experienced by a flat plate that is undergoing both translational and rotational motion in an unbounded fluid. Dimensional variables are used in this appendix.

A.1. *Unsteady Bernoulli equation for a flat plate with rotation*

We begin with the Euler equations for incompressible flow,

$$\frac{\partial \boldsymbol{u}}{\partial t} + (\boldsymbol{\nabla} \times \boldsymbol{u}) \times \boldsymbol{u} = -\boldsymbol{\nabla}\left(\frac{P}{\rho} + \frac{1}{2}|\boldsymbol{u}|^2\right), \quad \boldsymbol{\nabla} \cdot \boldsymbol{u} = 0, \tag{A1a,b}$$

where $\boldsymbol{u}$ is the velocity field, P is the pressure field, ρ is the fluid density and t is time. For an unsteady rotating flow in the dimensional Cartesian (x, y)-plane (different from the dimensionless Cartesian frame of § 2.1), the velocity field can be generally expressed as

$$\boldsymbol{u} = \boldsymbol{\nabla}\phi + \boldsymbol{\Omega} \times \boldsymbol{x}, \tag{A2}$$

where $\boldsymbol{x} = x\boldsymbol{i} + y\boldsymbol{j}$, ϕ is the (real-valued) velocity potential, the angular velocity due to rigid body rotation about the Cartesian z-axis (not to be confused with the complex z-plane) is

$$\boldsymbol{\Omega} = \Omega_0(t)\boldsymbol{k}, \tag{A3}$$

with $\Omega_0(t)$ being a specified function of time, and $\boldsymbol{i}, \boldsymbol{j}$ and $\boldsymbol{k}$ are the basis vectors in the x-, y- and z-directions, respectively. The centre of rotation is allowed to move in time, by

replacing $\boldsymbol{x}$ with $\boldsymbol{x} - \boldsymbol{x}_c(t)$. The extra term, $-\boldsymbol{\Omega} \times \boldsymbol{x}_c(t)$ may then simply be absorbed into ϕ and can hence be ignored in the analysis.

Following the usual derivation of Bernoulli's equation, the momentum equation in (A1*a*,*b*) becomes

$$\boldsymbol{u} \cdot \left(\frac{\partial \boldsymbol{\Omega}}{\partial t} \times \boldsymbol{x} \right) = -\boldsymbol{u} \cdot \boldsymbol{\nabla} \left(\frac{P}{\rho} + \frac{1}{2}|\boldsymbol{u}|^2 + \frac{\partial \phi}{\partial t} \right). \tag{A4}$$

The unsteady Bernoulli equation,

$$\frac{P}{\rho} + \frac{1}{2}|\boldsymbol{u}|^2 + \frac{\partial \phi}{\partial t} = C, \tag{A5}$$

is recovered when the left-hand side of (A4) vanishes, i.e. C is constant on any individual streamline. The left-hand side of (A4) vanishes for steady rotation, i.e. $\Omega_0(t)$ is independent of time, but this left-hand side is generally non-zero for unsteady rotation. However, a flat plate is a special case.

Consider the two-dimensional rotating flow about a flat plate that intersects the origin. On the plate boundary, the vectors $\boldsymbol{x}$ and $\boldsymbol{u}$ are parallel to the plate because of its no-penetration condition. It then follows that the left-hand side of (A4) vanishes and (A5) holds on the plate boundary. This is the result we seek and shows that the Bernoulli equation can be used on the plate boundary.

Finally, we note that on the plate boundary,

$$\boldsymbol{u} \cdot (\boldsymbol{\Omega} \times \boldsymbol{x}) = \boldsymbol{0}, \tag{A6}$$

and so

$$-\boldsymbol{\nabla}\phi \cdot (\boldsymbol{\Omega} \times \boldsymbol{x}) = |\boldsymbol{\Omega} \times \boldsymbol{x}|^2, \tag{A7}$$

on the plate boundary. This identity is used in the next section to calculate the aerodynamic force experienced by the flat plate.

A.2. *Aerodynamic force on a flat plate*

The force on the flat plate is

$$\boldsymbol{F} = \oint_{S_B} p\boldsymbol{n}\, \mathrm{d}s, \tag{A8}$$

where $\boldsymbol{n}$ is the inward pointing normal and S_B is the plate boundary; see figure 7. Substituting the Bernoulli equation (A5) into (A8), and making use of (A2), gives

$$\boldsymbol{F} = -\rho \oint_{S_B} \left(\frac{\partial \phi}{\partial t} + \frac{1}{2}|\boldsymbol{\nabla}\phi + \boldsymbol{\Omega} \times \boldsymbol{x}|^2 \right) \boldsymbol{n}\, \mathrm{d}s, \tag{A9}$$

which, upon using (A7) and the fact that $|\boldsymbol{\Omega} \times \boldsymbol{x}|$ is continuous across the plate, reduces to

$$\boldsymbol{F} + \rho \oint_{S_B} \left(\frac{\partial \phi}{\partial t} + \frac{1}{2}|\boldsymbol{\nabla}\phi|^2 \right) \boldsymbol{n}\, \mathrm{d}s = 0. \tag{A10}$$

We work in the frame in which the flow is stationary far from the flat plate. The plate moves and the centre of rotation always lies on the plate. Consider the contours shown in figure 7, where $S_{V_n}(t)$ with $n = 1, 2$, is the contour surrounding and adjacent to the n-vortex sheet, whereas $S_\infty(t)$ is the far-field contour that encompasses the whole flow.

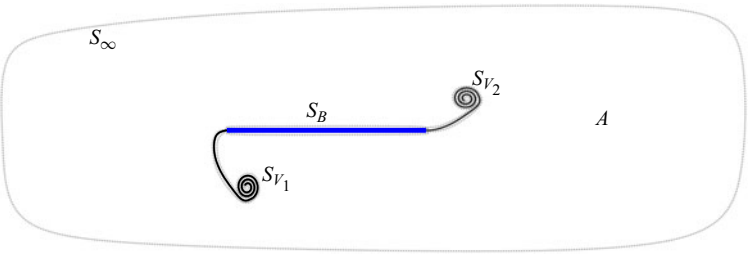

Figure 7. Contours and areal region used in Appendix A.2 to calculate the aerodynamic force on a flat plate that is translating and rotating in a fluid. The flat plate is coloured blue, the vortex sheets from the leading and trailing edges are solid black lines, whereas the contours used in the integrations are dotted black lines.

The areal region between the plate, the vortex sheets and the far-field contour is denoted $A(t)$.

The Reynolds transport theorem furnishes

$$\rho\frac{\mathrm{d}}{\mathrm{d}t}\int\limits_{S_B+S_V+S_\infty}\phi\boldsymbol{n}\,\mathrm{d}s=\rho\frac{\mathrm{d}}{\mathrm{d}t}\iint_A\nabla\phi\,\mathrm{d}A, \tag{A11a}$$

$$=\rho\iint_A\nabla\left(\frac{\partial\phi}{\partial t}\right)\mathrm{d}A+\rho\int_{S_B+S_V+S_\infty}\frac{\partial\phi}{\partial n}\nabla\phi\,\mathrm{d}s, \tag{A11b}$$

$$=\rho\int_{S_B+S_V+S_\infty}\frac{\partial\phi}{\partial t}\boldsymbol{n}+\frac{\partial\phi}{\partial n}\nabla\phi\,\mathrm{d}s, \tag{A11c}$$

where $S_V=S_{V_1}+S_{V_2}$ denotes union of the contours around the vortex sheets. Because S_∞ is stationary, we obtain

$$\begin{aligned}\rho\frac{\mathrm{d}}{\mathrm{d}t}\int_{S_V}\phi\boldsymbol{n}\,\mathrm{d}s+\rho\frac{\mathrm{d}}{\mathrm{d}t}\int_{S_B}\phi\boldsymbol{n}\,\mathrm{d}s&=\rho\int_{S_V}\frac{\partial\phi}{\partial t}\boldsymbol{n}\,\mathrm{d}s+\rho\int_{S_B}\frac{\partial\phi}{\partial t}\boldsymbol{n}\,\mathrm{d}s\\&\quad+\rho\int_{S_B}\frac{\partial\phi}{\partial n}\nabla\phi\,\mathrm{d}s+\rho\int_{S_V}\frac{\partial\phi}{\partial n}\nabla\phi\,\mathrm{d}s\\&\quad+\rho\int_{S_\infty}\frac{\partial\phi}{\partial n}\nabla\phi\,\mathrm{d}s.\end{aligned} \tag{A12}$$

Next, we note that

$$\rho\int_{S_B}\frac{\partial\phi}{\partial n}\nabla\phi-\frac{1}{2}|\nabla\phi|^2\boldsymbol{n}\,\mathrm{d}s=-\rho\int_{S_V+S_\infty}\frac{\partial\phi}{\partial n}\nabla\phi-\frac{1}{2}|\nabla\phi|^2\boldsymbol{n}\,\mathrm{d}s. \tag{A13}$$

Adding (A10) to (A12) and applying the relation in (A13), gives

$$\boldsymbol{F}+\rho\frac{\mathrm{d}}{\mathrm{d}t}\int_{S_B+S_V}\phi\boldsymbol{n}\,\mathrm{d}s=\rho\int_{S_V+S_\infty}\left(\frac{\partial\phi}{\partial t}+\frac{1}{2}|\nabla\phi|^2\right)\boldsymbol{n}\,\mathrm{d}s. \tag{A14}$$

We can now show that the right-hand side of (A14) vanishes.

On S_V, the integrand of (A14) is $\mathrm{D}\Gamma/\mathrm{D}t$, where the circulation Γ is the jump in potential across the sheet. The circulation is an invariant of the sheet motion, i.e. $\mathrm{D}\Gamma/\mathrm{D}t=0$. Far from the plate, $\nabla\phi\sim\partial\phi/\partial n\sim 1/r^2$, and so the integral over S_∞ in the right-hand side

of (A14) decays as r^{-3} and, hence, vanishes as $r \to \infty$. Then the force can be determined from (A14) to give

$$\boldsymbol{F} = (F_x, F_y) = -\rho \frac{\mathrm{d}}{\mathrm{d}t} \int_{S_B+S_V} \phi \boldsymbol{n} \, \mathrm{d}s, \tag{A15}$$

which can be complexified to obtain

$$F_y - \mathrm{i}F_x = -\rho \frac{\mathrm{d}}{\mathrm{d}t} \int_{\mathcal{C}(t)} w(z) \, \mathrm{d}z, \tag{A16}$$

where $w = \phi + \mathrm{i}\psi$ is the complex velocity potential, because the stream function, ψ, is constant on the body and it is continuous across the vortex sheets. We have written $\mathcal{C}(t) = S_B + S_V$, which is the contour that encloses and is adjacent to the plate and the vortex sheets. We then revert back to the moving frame of the plate, and account for the moving centre of rotation (see § A.1), to obtain

$$F_y - \mathrm{i}F_x = -\rho \frac{\mathrm{d}}{\mathrm{d}t} \int_{\mathcal{C}(t)} w(z) - w_\infty(z) - w_R(z) \, \mathrm{d}z, \tag{A17}$$

where $w_\infty(z)$ accounts for flow at infinity, $w_R(z) = -\mathrm{i}\bar{z}_R(t)z$, and $\bar{z}_R(t)$ is the centre of rotation moving with the flow. We note that the integrals of both $w_\infty(z)$ and $w_R(z)$ vanish, giving the required result,

$$F_y - \mathrm{i}F_x = -\rho \frac{\mathrm{d}}{\mathrm{d}t} \int_{\mathcal{C}(t)} w(z) \, \mathrm{d}z. \tag{A18}$$

References

Alexander, R.C. 1971 Family of similarity flows with vortex sheets. *Phys. Fluids* **14** (2), 231–239.

Baddoo, P.J. & Ayton, L.J. 2018 Potential flow through a cascade of aerofoils: direct and inverse problems. *Proc. R. Soc. Lond.* A **474** (2217), 20180065.

Baddoo, P.J., Kurt, M., Ayton, L.J. & Moored, K.W. 2020 Exact solutions for ground effect. *J. Fluid Mech.* **891**, R2.

Batchelor, G.K. 1967 *An Introduction to Fluid Dynamics*. Cambridge University Press.

Birkhoff, G. 1962 Helmholtz and Taylor instability. In *Proceedings of Symposia in Applied Mathematics*, vol. 13, pp. 55–76. American Mathematical Society.

Cortelezzi, L. & Leonard, A. 1993 Point vortex model of the unsteady separated flow past a semi-infinite plate with transverse motion. *Fluid Dyn. Res.* **11** (6), 263–295.

Crighton, D.G. 1985 The Kutta condition in unsteady flow. *Annu. Rev. Fluid Mech.* **17**, 411–445.

Eldredge, J.D. 2007 Numerical simulation of the fluid dynamics of 2D rigid body motion with the vortex particle method. *J. Comput. Phys.* **221** (2), 626–648.

Gharib, M., Rambod, E. & Shariff, K. 1998 A universal time scale for vortex ring formation. *J. Fluid Mech.* **360**, 121–140.

Graham, J.M.R. 1983 The lift on an aerofoil in starting flow. *J. Fluid Mech.* **133**, 413–425.

Jones, A.R. & Babinsky, H. 2010 Unsteady lift generation on rotating wings at low Reynolds numbers. *J. Aircraft* **47** (3), 1013–1021.

Jones, M.A. 2003 The separated flow of an inviscid fluid around a moving flat plate. *J. Fluid Mech.* **496**, 405–441.

Kaden, H. 1931 Aufwicklung einer unstabilen unstetigkeitsfläche. *Ing.-Arch.* **2** (2), 140–168.

Krasny, R. & Nitsche, M. 2002 The onset of chaos in vortex sheet flow. *J. Fluid Mech.* **454**, 47–69.

Luchini, P. & Tognaccini, R. 2002 The start-up vortex issuing from a semi-infinite flat plate. *J. Fluid Mech.* **455**, 175–193.

Milne-Thomson, L.M. 1996 *Theoretical Hydrodynamics*. Courier Corporation.

Moore, D.W. 1975 The rolling up of a semi-infinite vortex sheet. *Proc. R. Soc. Lond.* A **345** (1642), 417–430.

Pitt Ford, C.W. & Babinsky, H. 2013 Lift and the leading-edge vortex. *J. Fluid Mech.* **720**, 280–313.

Prandtl, L. 1921 Applications of modern hydrodynamics to aeronautics. *NACA Tech. Rep.* 116, pp. 157–215.

PULLIN, D.I. 1978 The large-scale structure of unsteady self-similar rolled-up vortex sheets. *J. Fluid Mech.* **88** (3), 401–430.

PULLIN, D.I. & PERRY, A.E. 1980 Some flow visualization experiments on the starting vortex. *J. Fluid Mech.* **97** (2), 239–255.

PULLIN, D.I. & SADER, J.E. 2021 On the starting vortex generated by a translating and rotating flat plate. *J. Fluid Mech.* **906**, A9.

PULLIN, D.I. & WANG, Z.J. 2004 Unsteady forces on an accelerating plate and application to hovering insect flight. *J. Fluid Mech.* **509**, 1–21.

ROTT, N. 1956 Diffraction of a weak shock with vortex generation. *J. Fluid Mech.* **1** (1), 111–128.

SADER, J.E., HOU, W., HINTON, E.M., COLONIUS, T. & PULLIN, D.I. 2024 The starting vortices generated by bodies with sharp and straight edges in a viscous fluid. *J. Fluid Mech.* (submitted).

SAFFMAN, P.G. 1995 *Vortex Dynamics*. Cambridge University Press.

SCHMITZ, F.W. 1941 *Aerodynamics of the Model Airplane. Part 1. Airfoil Measurements*. Redstone Scientific Information Center.

TCHIEU, A.A. & LEONARD, A. 2011 A discrete-vortex model for the arbitrary motion of a thin airfoil with fluidic control. *J. Fluids Struct.* **27** (5–6), 680–693.

WAGNER, H. 1925 Über die entstehung des dynamicshen auftriebes von tragflügeln. *Z. Angew. Math. Mech.* **5**, 17–35.

WINSLOW, J., OTSUKA, H., GOVINDARAJAN, B. & CHOPRA, I. 2018 Basic understanding of airfoil characteristics at low Reynolds numbers (10^4–10^5). *J. Aircraft* **55** (3), 1050–1061.

XU, L. & NITSCHE, M. 2015 Start-up vortex flow past an accelerated flat plate. *Phys. Fluids* **27** (3), 033602.